Enhancing the Carrier Transport in Monolayer MoS2 Through Interlayer Coupling with 2D Covalent Organic Frameworks

Can Wang, Luca Cusin, Chun Ma, Elif A Unsal, Hanlin Wang, Valentina Girelli Consolaro, Verónica Montes-garcía, Bin Han, Stefania Vitale, Arezoo Dianat, et al.

ADVANCED MATERIALS
www.advmat.de

Enhancing the Carrier Transport in Monolayer MoS_2 through Interlayer Coupling with 2D Covalent Organic Frameworks

*Can Wang, Luca Cusin, Chun Ma, Elif Unsal, Hanlin Wang, Valentina Girelli Consolaro, Verónica Montes-García, Bin Han, Stefania Vitale, Arezoo Dianat, Alexander Croy, Haiming Zhang, Rafael Gutierrez, Gianaurelio Cuniberti, Zhaoyang Liu, Lifeng Chi, Artur Ciesielski, and Paolo Samorì**

The coupling of different 2D materials (2DMs) to form van der Waals heterostructures (vdWHs) is a powerful strategy for adjusting the electronic properties of 2D semiconductors, for applications in opto-electronics and quantum computing. 2D molybdenum disulfide (MoS_2) represents an archetypical semiconducting, monolayer thick versatile platform for the generation of hybrid vdWH with tunable charge transport characteristics through its interfacing with molecules and assemblies thereof. However, the physisorption of (macro)molecules on 2D MoS_2 yields hybrids possessing a limited thermal stability, thereby jeopardizing their technological applications. Herein, the rational design and optimized synthesis of 2D covalent organic frameworks (2D-COFs) for the generation of MoS_2/2D-COF vdWHs exhibiting strong interlayer coupling effects are reported. The high crystallinity of the 2D-COF films makes it possible to engineer an ultrastable periodic doping effect on MoS_2, boosting devices' field-effect mobility at room temperature. Such a performance increase can be attributed to the synergistic effect of the efficient interfacial electron transfer process and the pronounced suppression of MoS_2's lattice vibration. This proof-of-concept work validates an unprecedented approach for the efficient modulation of the electronic properties of 2D transition metal dichalcogenides toward high-performance (opto)electronics for CMOS digital circuits.

1. Introduction

2D transition metal dichalcogenides (2D TMDCs) are emerging as prototypical 2D semiconductors for applications in high-performance opto-electronic devices. Among them, molybdenum disulfide (MoS_2) is the most explored TMDCs because it combines high mechanical robustness, strong spin–orbit coupling with favorable electronic and optical properties. Such unique characteristics render MoS_2 a promising candidate in both fundamental research and practical applications beyond (opto)electronics in the field of energy conversion and storage as well as chemical and physical sensing.[1] In particular, the high degree of electrostatic control makes MoS_2 ideal channel material in field-effect transistors (FETs), whose functional complexity can be further enhanced by chemical functionalization, epitomizing a More-than-Moore strategy in the post-silicon era.[2]

However, the recent development of MoS_2-based high-end electronics is still

C. Wang, Z. Liu
State Key Laboratory of Supramolecular Structure and Materials
Jilin University
Changchun 130012, P. R. China

C. Wang, L. Cusin, C. Ma, H. Wang, V. Montes-García, B. Han, S. Vitale, A. Ciesielski, P. Samorì
Institut de Science et d'Ingénierie Supramoléculaires (ISIS)
Université de Strasbourg & CNRS
8 allée Gaspard Monge, Strasbourg 67000, France
E-mail: samori@unistra.fr

The ORCID identification number(s) for the author(s) of this article can be found under https://doi.org/10.1002/adma.202305882

DOI: 10.1002/adma.202305882

E. Unsal, A. Dianat, R. Gutierrez, G. Cuniberti
Institute for Materials Science and Max Bergmann Center of Biomaterials
TU Dresden
01062 Dresden, Germany

V. G. Consolaro
IPCMS
UMR 7504 CNRS
Université de Strasbourg
23 rue du Loess, Strasbourg 67034, France

A. Croy
Institute of Physical Chemistry
Friedrich Schiller University Jena
07737 Jena, Germany

H. Zhang, L. Chi
Institute of Functional Nano & Soft Materials (FUNSOM)
Jiangsu Key Laboratory for Carbon Based Functional Materials & Devices
Soochow University
Suzhou 215123, P. R. China

hampered by the significantly limited charge transport properties, e.g., most of the reported electron mobilities (approximately tens of $cm^2\ v^{-1}\ s^{-1}$) in backgated MoS_2 FETs at room temperature are much lower than the theoretically predicted values (≈410 $cm^2\ v^{-1}\ s^{-1}$),[3] mainly because of the undesired collective effects of structural defects and the presence of impurities (either environmental or those introduced during the processing), ultimately jeopardizing their applications.[4] Therefore, improving the charge transport in monolayer MoS_2 via noninvasive approaches is highly sought after.

Passivation by layered hexagonal boron nitride (hBN),[5] inorganic materials (such as HfO_2,[6] Al_2O_3,[7] and CaF_2),[8] organic molecule modification, or even doping strategy are effective methods to improve TMDCs devices' performances. Compared to the time-consuming dry transfer procedure for hBN and atomic layer deposition (ALD) technique commonly used with inorganic materials, the passivation with small organic molecules represents a simpler, more versatile, and cheaper approach. For example, interfacing of TMDCs with organic molecules featuring electron-donating/withdrawing groups can lead to doping of the semiconductor through the controlled local modification of its surface potential.[9] More importantly, the doping intensity can be amplified via cooperative effects when molecules self-assemble onto 2DMs nanosheets into ordered supramolecular structures.[10] However, 2D supramolecular structures held together by noncovalent interactions undergo dynamic rearrangements upon humidity or high-temperature exposure,[11] which lead to instabilities in 2DM-based (opto)electronic devices under operation. In this regard, the use of more robust interactions tethering the molecular units into crystalline films with long-range order is highly desirable.

2D covalent organic frameworks (2D-COFs) are a new class of crystalline organic materials composed of 2D polymer sheets featuring an ordered structure, defined porosity, high surface area, and easy chemical tunability.[12] 2D-COFs thin films with long-range order along the in-plane directions are particularly appealing and can be produced via interfacial synthesis where the reaction is constrained in a 2D space.[13] Unlike self-assembled structures, COFs exhibit much higher thermal and chemical stability owing to the covalent nature of their architectures. The great variety of starting building units and covalent linkages enables the bottom-up engineering of the COF surface areas, pore sizes, and crystal structure. During the initial stages of development, various COFs with reasonable conductivities were generated exploiting organic nodes connected by B—O bonds.[14] However, the incorporation of conductive and conjugated ligand units in these B—O-linked 2D-COFs resulted in a limited range of conductivities that are still lower than those achieved by other high-performance conducting polymers. In 2011, the development of conductive 2D-COF with imine linkages was reported as COF-366,[15] which was found to provide carrier mobilities that were almost as good as polycrystalline silicon. Since then, other bond connections such as triazine, hydrazine, and azine linkages have been explored to synthesize 2D-COFs with improved electrical conductivities. These linkages typically contain heteroatoms, which contribute to the structural polarity of the 2D-COFs. This bond polarization has a significant impact on the stacking behavior of the layered sheets in 2D-COFs, ultimately affecting their charge transport performance. Overall, conjugated 2D-COFs are not ideal as transport layers since most of them are wide bandgap semiconductors, however by taking into account their well-defined structural features in combination with their good mechanical stiffness,[16] their hybridization with a 2D semiconductor can represent a powerful strategy to exploit their chemical programmability for realizing a novel generation of robust hybrid organic/inorganic van der Waals heterostructures (vdWHs).[17]

In this work, we have synthesized imine-based 2D-COFs via Schiff-base reaction at the water/air interface[18] and transferred them onto monolayer MoS_2 flakes. The charge carrier density of MoS_2 enhanced significantly through the interlayer coupling with 2D-COFs, exceeding $10^{12}\ e^-\ cm^{-2}$. Density functional theory (DFT) calculations revealed an upward shift of MoS_2's Fermi level (E_F) thereby indicating the efficient charge transfer from 2D-COF film to MoS_2. More importantly, temperature-dependent photoluminescence (PL) spectra suggest that the coupling with 2D-COFs is accompanied with a decrease in the optical phonon energy of MoS_2, which demonstrates the suppression of the phonon–electron scattering effects in MoS_2 lattice in the vdWHs, leading to a larger population of free carriers. Overall, the synergistic effect of the efficient electron transfers and the suppression of MoS_2's lattice vibration contributes to the boosting of the electron mobility[19] at room temperature in our MoS_2 /2D-COF hybrid heterostructures.

2. Results and Discussion

2.1. 2D-COF Thin-Film Synthesis and Characterization

The imine-linked 2D-COF thin films were synthesized at water–air interface by combining the 1,3,5-*tris*(4-aminophenyl)benzene (TAPB) unit with 1,3,5-*tris*(4-formylphenyl)benzene (TFPB)[20] or terephthaldehyde (PDA).[21] Solutions of the two monomers in chloroform were spread onto water surface in a Langmuir trough and then compressed by means of movable lateral barriers. The water subphase contained scandium trifoliate acting as catalyst for the Schiff-base reaction[22] (Figure S1, Supporting Information). The free-standing 2D-COF films were transferred by the Langmuir–Schaefer (LS) method onto a Si/SiO_2 substrate, as shown in **Figure 1**a. The transferred 2D-COF films were rinsed with water and isopropanol to remove the excess of catalyst and unreacted monomers. Figure 1b portrays the optical microscopy image of the homogenous 2D-COF TAPB-PDA film featuring a crack formed during the transfer process. Topographic atomic force microscopy (AFM) images of the film edge revealed a thickness of 3.7 and 3.6 nm for the 2D-COF TAPB-TFPB and 2D-COF TAPB-PDA films, respectively (Figure S2, Supporting Information). Due to the tip-sample convolution effect and surface roughness of substrate (≈0.1 nm for SiO_2), the film thickness measured by AFM is typically higher (≈0.8 nm) than the theoretical value (≈0.47 nm)[23] of a MoS_2 monolayer.[16b,22] The environmental humidity (≈60%) also affected the thickness in AFM measurements, as high relative humidity leads to a large

G. Cuniberti
Dresden Center for Computational Materials Science (DCMS)
TU Dresden
01062 Dresden, Germany

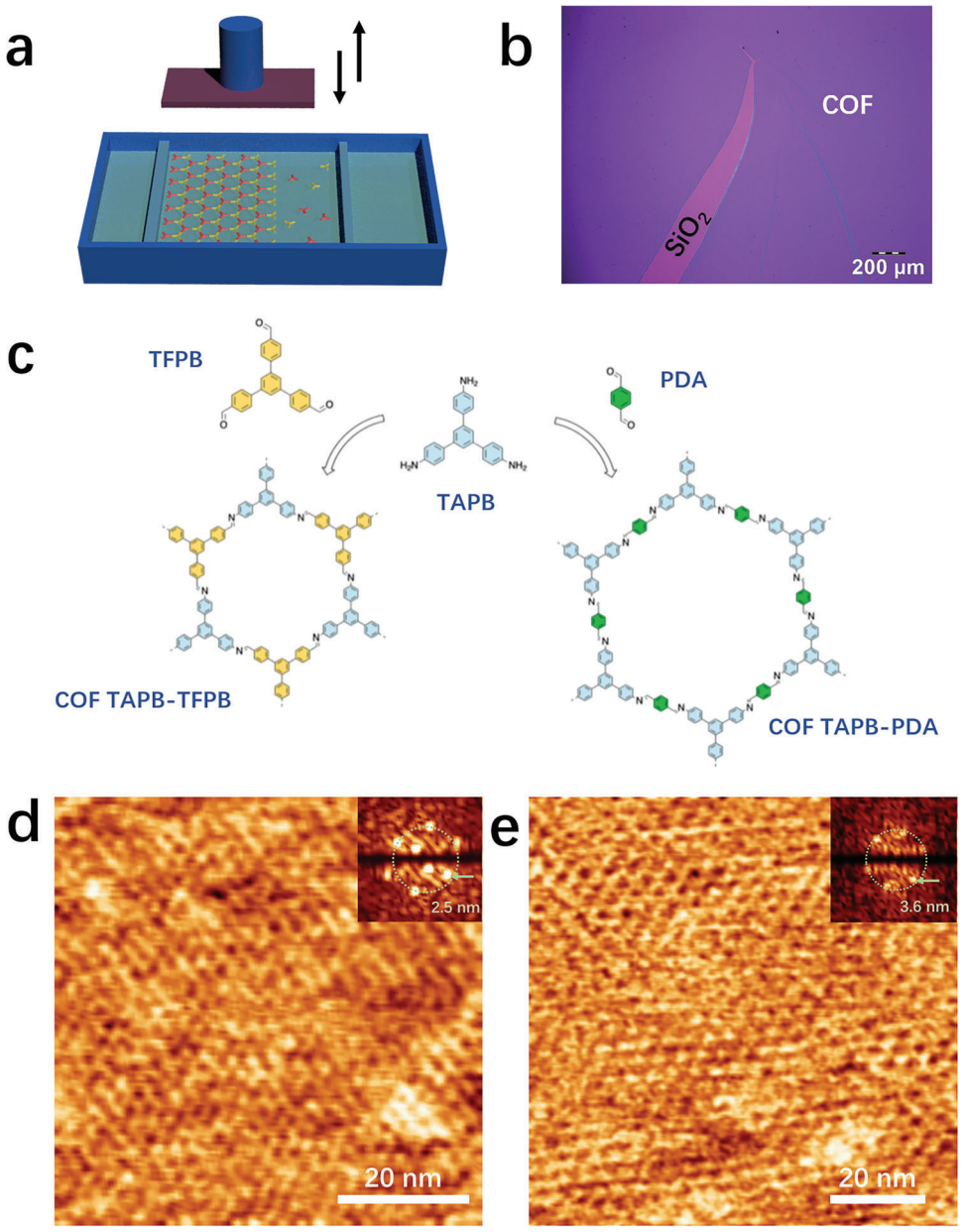

Figure 1. a) Schematic illustration of the 2D-COF film synthesis and the Langmuir–Schaefer (LS) transfer method. b) Optical microscopy image of the 2D-COF TAPB-PDA film deposited onto Si/SiO_2 substrate. c) Chemical structures of 2D-COF TAPB-TFPB and 2D-COF TAPB-PDA. d,e) Constant current STM image of d) 2D-COF TAPB-TFPB and e) 2D-COF TAPB-PDA film on Au (111) surface. Tunneling parameters: d) tip bias voltage (V_t) = 500 mV, average tunneling current (I_t) = 60 pA; e) V_t = 365 mV, I_t = 60 pA.

adhesion force between the tip and hydrophilic surface.[24] We estimated that our 2D-COF films were about five atomic layers' thick. Moreover, the few-layer thick 2D-COF films displayed an extremely flat surface with a root mean square roughness (R_{RMS}) of 0.237 and 0.278 nm as estimated on 100 μm^2 area, for 2D-COF TAPB-TFPB and 2D-COF TAPB-PDA, respectively. Remarkably, our 2D-COF films have good thermal stability, with unchanged structure after annealing at 520 K.[25] The small roughness made our 2D-COF films good candidates for building vdWHs though their interfacing with 2D materials. The obtained 2D-COF thin films were found being robust enough during the transfer steps covering almost the entire transmission electron microscope (TEM) grids, showcasing their excellent mechanical robustness (Figure S3, Supporting Information). As the freestanding 2D-COF thin films were highly sensitive to the electron beam irradiation, the TEM samples got deteriorated rapidly and no high-resolution image of the ordered structure could be acquired. To enhance the radiation resistance of the 2D-COF films, a sandwich structure of 2D-COF film encapsulated in-between two layers of chemical vapor deposition (CVD) graphene was assembled. To this end, selected area electron diffraction was performed with low-dose diffraction technique. As shown in Figure S4 in

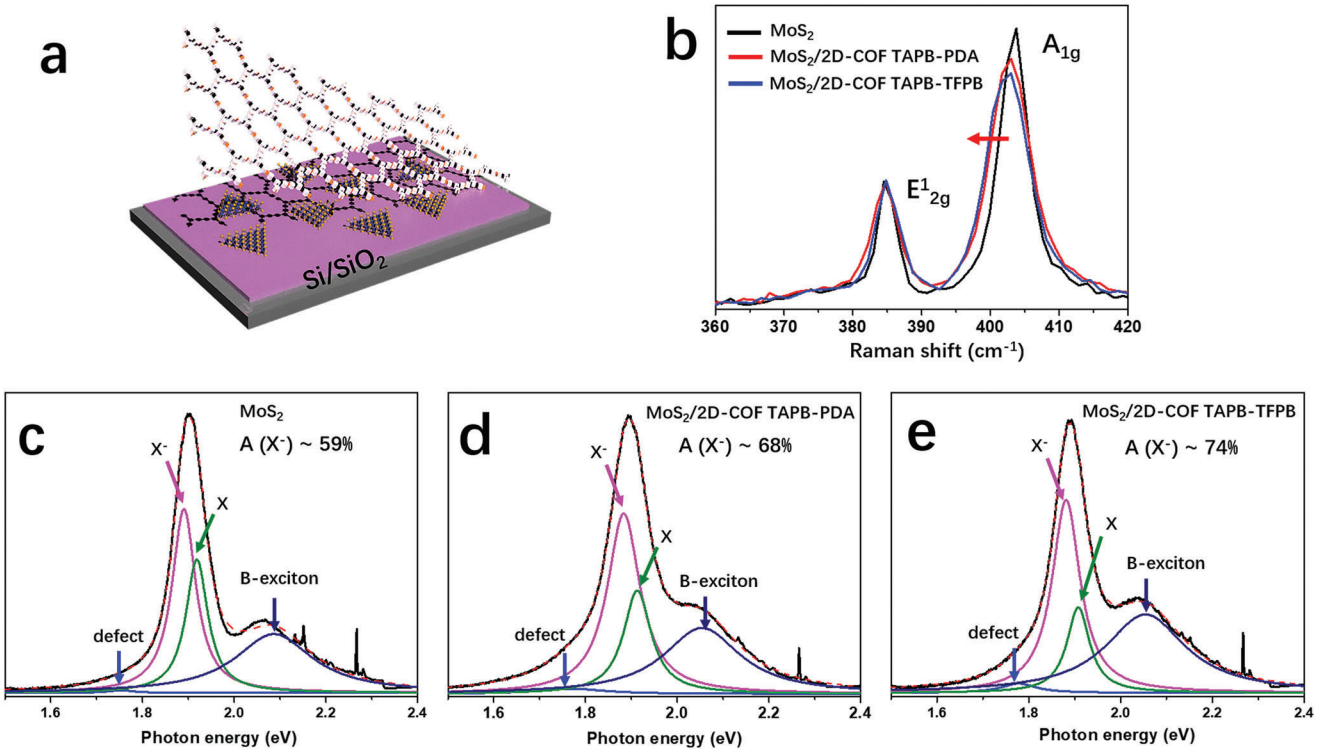

Figure 2. a) Schematic representation of MoS_2/2D-COF vdWH formation. b) Raman spectra of bare MoS_2 and vdWHs measured at room temperature. Photoluminescence (PL) spectra at 77 K of c) bare MoS_2, d) MoS_2/2D-COF TAPB-TFPB vdWH, e) MoS_2/2D-COF TAPB-PDA vdWH, fitted with a Lorentzian function to quantify the trion (X^-) weight at 1.88 eV.

the Supporting Information, two rings composed of clear diffraction spots were observed from the sandwich-structured samples. The diffraction spots at around 8.1 and 4.5 nm^{-1} were attributed to the reflections of (110) graphene and the cavity of the benzene units,[16b] suggesting a high degree of order within the 2D-COF films. The porous crystalline structure of 2D-COF films physisorbed on Au (111) substrate was monitored with a sub-nm resolution by scanning tunneling microscopy (STM). Both 2D-COF films exhibited highly ordered in-plane structure, as shown in Figure 1d,e. The fast Fourier transform pattern revealed that the superlattice structure possessing a sixfold symmetry with a periodicity of ≈2.5 and ≈3.6 nm for 2D-COF TAPB-TFPB and 2D-COF TAPB-PDA, respectively. Moreover, the film rigidity was studied by AFM in force volume spectroscopy (Figure S7, Supporting Information), revealing that 2D-COF TAPB-TFPB film with a smaller periodicity exhibits a greater rigidity when compared to the 2D-COF TAPB-PDA film.

X-ray photoelectron spectroscopy (XPS) investigations were performed to gain insight into the chemical composition of the 2D-COF films.[26] The analysis of the N 1s peak (Figure S8, Supporting Information) confirmed that the N—NH_2 peak at ≈399.5 eV was highly reduced after Schiff-base condensation reaction. Meanwhile, the emergence of N—N=C peak at ≈398.8 eV indicated the formation of the target imine bond. The presence of a shoulder peak at higher energy level ≈400.5 eV can be ascribed to X-ray-oxidized nitrogen. By integrating the XPS peak areas, the yield of polymerization was estimated as 87% and 83% for the 2D-COF TAPB-PDA and the 2D-COF TAPB-TFPB, respectively. Moreover, surface-enhanced Raman scattering (SERS) spectroscopy was employed to gain additional information on the chemical structure of the obtained thin 2D-COF films[27] (Figure S9, Supporting Information). Compared with the building monomers, an additional shoulder peak appeared at ≈1550 cm^{-1}, near to the C=C vibration peak at ≈1600 cm^{-1} in case of both 2D-COF films, which can be attributed to the stretching vibration of the newly formed C=N bonds.[27a] Therefore, XPS and SERS results provided clear evidence for the formation of the targeted imine bond.

2.2. vdWHs Formation and the Interlayer Charge Transfer Process

Triangular CVD-grown MoS_2 flakes on sapphire substrate were first transferred onto a Si/SiO_2 substrate using polystyrene as supporting layer[28] (Figure S10, Supporting Information). The vdWHs were obtained by super-imposing the 2D-COF films directly onto the monolayer MoS_2 flakes (**Figure 2**a). AFM analysis revealed a complete coating of the monolayer MoS_2 triangle flakes with the 2D-COF film yielding the vdWHs (Figure S11, Supporting Information).

The formation of a hybrid organic–inorganic vdWHs allowed to finely tune the interfacial coupling between the adjacent layers, yielding a modulation of the electronic properties of the employed 2D materials. Compared with randomly physisorbed molecules, a tightly packed crystalline 2D-COF layer guaranteed

maximal interference on the band structure of MoS_2 via collective effects, by means of uniform doping. The energy levels of the frontier orbitals of these two 2D-COF films were studied by cyclic voltammetry measurements and compared to the results of UV-vis spectra (Figure S12, Supporting Information). The measured electrochemical bandgap of 2D-COF films was quite similar to the optical bandgap. In particular, the highest occupied molecular orbital/lowest unoccupied molecular orbital levels of the 2D-COF films resulted −5.32 eV/−2.44 eV and −5.28 eV/−2.62 eV for TAPB-TFPB and TAPB-PDA 2D-COFs, respectively. Conversely, the valence band and conduction band of monolayer MoS_2 amounted to −5.76 and −4.06 eV. Hence, in view of the higher electron affinity of the 2D semiconductor, an electron transfer from both 2D-COF films to the MoS_2 could be expected. Indeed, Raman and PL spectroscopies (Figure S14, Supporting Information)[29] provided unambiguous evidence for the occurrence of such charge transfer. In particular, Raman spectra recorded at room temperature revealed that the out-of-plane vibration (A_{1g}) peak of MoS_2 shifts toward a lower energy region in the vdWHs, while the in-plane vibration ($E^1{}_{2g}$) mode location remained constant (Figure 2b). The $E^1{}_{2g}$ mode at 386 cm^{-1} and A_{1g} mode at 404 cm^{-1} displayed <20 cm^{-1} difference, confirming a monolayer nature of MoS_2. We normalized the intensity of $E^1{}_{2g}$ peaks and compared the change of the of A_{1g} peak positions between pristine MoS_2 and vdWHs. The interfacing of the 2D semiconductor with 2D-COF TAPB-PDA resulted in ≈1 cm^{-1} redshift of the A_{1g} peak with a decrease in peak intensity, indicating the occurrence of charge transfer occurs from the 2D-COF film to the MoS_2 layer (n-doping effect). A similar phenomenon was observed in MoS_2/2D-COF TAPB-TFPB vdWHs, where the changes of A_{1g} peak position were found being more pronounced (≈1.1 cm^{-1}), indicating a higher surface electron concentration of MoS_2. The electron doping level of monolayer MoS_2 can be quantified via low-temperature PL spectra. With the decreasing temperature, the electron–phonon scattering in MoS_2 crystal lattice became weaker, yielding a more pronounced PL from localized exciton emission. For a typical PL spectrum of monolayer MoS_2 at 77 K (Figure 2c), a strong emission feature associated with the optical transitions between the highest valence band and the conduction band at the K-points referred to as the ground state A-exciton emission at ≈1.90 eV. Because of the spin–orbit splits of the valence band, secondary emission peak with weaker intensity appeared at a higher energy ≈2.10 eV, which is referred to as the B-exciton peak. The A-exciton peak could be deconvoluted into three peaks after Lorentzian fitting, including defect-related peak at a lower energy ≈1.76 eV, neutral exciton (X) at ≈1.91 eV, and trion peak (X^-) at ≈1.88 eV. The negatively charged trion was formed upon photogenerated exciton binding to free electron with a binding energy around 30 meV.[30] Hence, the spectral weight of trion was related to the doping level of MoS_2. As shown in Figure 2c–e, the presence of 2D-COF films increased the trion weight by 9% and 15% in the case of COF TAPB-PDA and TAPB-TFPB vdWHs, respectively, featuring a characteristic n-type doping effect.

The doping of MoS_2 resulting from its interfacing with the 2D-COFs was further confirmed by XPS measurements. Figure S15 in the Supporting Information compares the binding energies of Mo 3d and S 2p core levels for pristine MoS_2 monolayer and two MoS_2/2D-COF vdWHs. The binding energies of both elements resulted being shifted upward by about 0.1 eV in MoS_2/2D-COF TAPB-PDA heterostructure, and about 0.2 eV in MoS_2/2D-COF TAPB-TFPB heterostructure. The upward shift of binding energy indicated that MoS_2's Fermi level moves toward the conduction band.[31] Our XPS characterizations further demonstrated the n-type doping effect of MoS_2 in the vdWHs, corroborating the Raman and PL results.

2.3. Electrical Characterization and Band Structure Simulation

To bestow information on the band structure alignment caused by charge transfer process, the electrical characteristics of the CVD MoS_2-based films were investigated by constructing FETs. Back-gate monolayer MoS_2 devices were fabricated by using thermally evaporated top Au electrodes, which exhibit Ohmic contact at room temperature. It is worth noting that the mixed monomer films limited the devices' current with a weak p-doping effect (Figure S16, Supporting Information), while the covalently bonded 2D-COF films yielded an improvement in the devices' performance. **Figure 3**a,b compared the representative gate-dependent transport characteristics of monolayer MoS_2 devices with source–drain bias at V_{DS} = 500 mV. The pristine carrier density (n_e) in MoS_2 could be extracted from the formula: $n_e = I_{DS}L/V_{DS}Wq\mu$. At V_{GS} = 0 V, n_e was calculated as 5.72×10^9 cm^{-2} (Figure 2a) and 2.42×10^9 cm^{-2} (Figure 2b). The transfer curves were monitored before and after the 2D-COF film physisorption, revealing a significant shift of the threshold voltage (V_{th}) toward negative V_{GS}. In particular, the source–drain current (I_{DS}) was greatly enhanced upon interfacing with 2D-COF films. The n-type doping effect could be quantified by the threshold voltage shift (ΔV_{th}), which is linearly proportional with the change of carrier densities (Δn) (Equation (2)). Here, ΔV_{th} was estimated to be 11 V for MoS_2/2D-COF TAPB-PDA and 16 V for MoS_2/2D-COF TAPB-TFPB, corresponding to a Δn of 1.04×10^{12} and 1.51×10^{12} cm^{-2}, respectively. The results recorded on five different devices for each vdWH type are summarized in Figures S18 and S19 in the Supporting Information, revealing a good reproducibility. Moreover, compared to the mixed monomers film, the MoS_2/2D-COF vdWH device still performed well after thermal annealing at 470 K (Figure S20, Supporting Information), hence being compatible to back-end integration process temperatures.

The ideal MoS_2/2D-COF vdWH superlattices were modeled using DFT, as shown in Figure S18a,b in the Supporting Information. The periodicity of these two 2D-COFs hexagonal lattice was simulated as 2.56 and 3.82 nm, in accordance with our STM results (Figure 1b,c). The different charge density images (Figure S21c,d, Supporting Information) indicated the electron transfer process from 2D-COF layer to MoS_2. The magnitude of electron transfer was calculated as 1.46×10^{12} cm^{-2} and 2.18×10^{12} cm^{-2} for TAPB-PDA and TAPB-TFPB containing MoS_2/2D COF vdWH, respectively. While the trend of the experimentally determined electron transfer values was in good agreement with the simulated ones, the former exhibited smaller absolute values because of the imperfect crystalline structure resulting from the interfacial synthesis of the 2D-COF films.

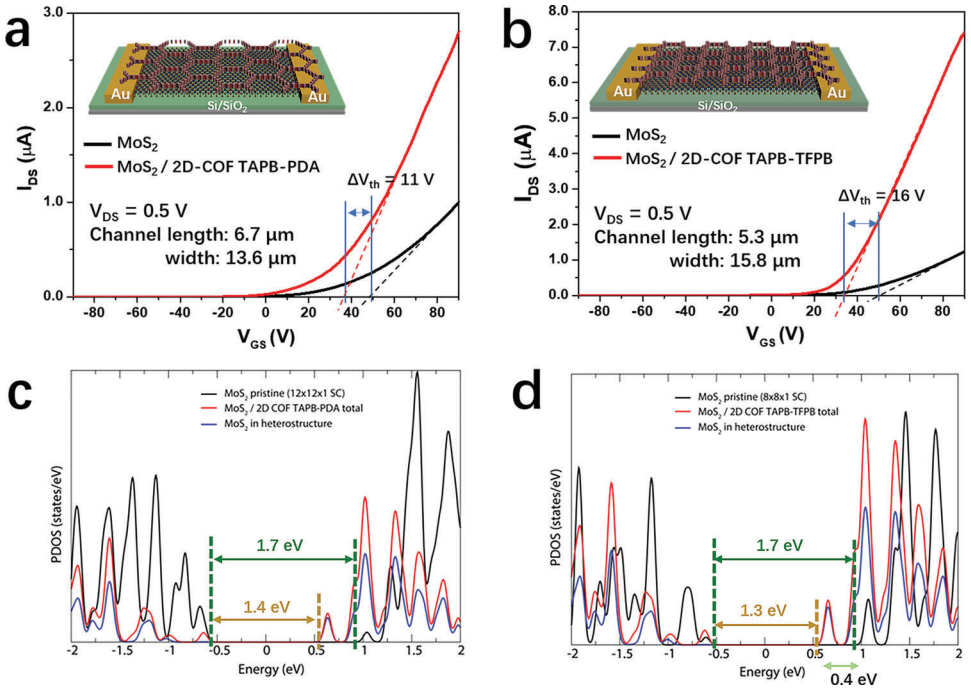

Figure 3. a,b) Transfer characteristics of pristine monolayer MoS_2 FET devices before (black line) and after (red line) interfacing with a) TAPB-PDA and b) TAPB-TFPB 2D-COF films. c,d) Density of states (DOS) of c) MoS_2/2D-COF TAPB-PDA, in 12 × 12 unit cell and d) MoS_2/2D-COF TAPB-TFPB, in 8 × 8 unit cell. Zero energy level is arbitrarily set to the middle of the band gap for comparison.

Alongside, the density of states (DOS) simulation also provided insight into the charge transfer process in the vdWHs, as shown in Figure 3c,d. The comparison of the DOS maps of MoS_2 before (black) and after (red) 2D-COF physisorption revealed an ≈0.3 eV energy shift toward lower energy values for MoS_2 conduction electrons in MoS_2/2D-COF TAPB-PDA heterostructure, and ≈0.4 eV in MoS_2/2D-COF TAPB-TFPB heterostructure. The shift of conduction band induced an increased probability of exciting electrons, confirming that the n-type doping on MoS_2 originates from the charge transfer effect of 2D-COF film. On the same time, the band gap (E_g) reduced from 1.7 eV (pristine MoS_2) to 1.4 and 1.3 eV for MoS_2/2D-COF TAPB-PDA and MoS_2/2D-COF TAPB-TFPB, respectively.

More importantly, the interlayer coupling of the CVD MoS_2 with the 2D-COF film led to a major relative enhancement of the field-effect electron mobility (μ) extracted from I_{DS}–V_{GS} curves (Equation (1)). Our unoptimized devices comprising the MoS_2/2D-COF TAPB-PDA heterostructure (Figure 3a) exhibited a μ of 9.8 $cm^2\ V^{-1}\ s^{-1}$, being notably larger than that in the pristine MoS_2 device (4.3 $cm^2\ V^{-1}\ s^{-1}$). Similarly, the dressing of MoS_2 with the 2D-COF TAPB-TFPB film increased the μ from 5.2 to 21.1 $cm^2\ V^{-1}\ s^{-1}$ (Figure 3b). The 2D-COF TAPB-TFPB could induce a much higher carrier mobility in monolayer MoS_2, which was also proved by simulation (Figure S23, Supporting Information). Moreover, coating both sides of MoS_2 with 2D-COF films can further optimize the device's performance by enhancing the electron transfer process (Figure S24, Supporting Information). The observed relative enhancement in field-effect mobility is noteworthy since typically the electron doping of MoS_2 resulting from its interfacing with a thin physisorbed organic molecular film was accompanied by a more modest increase in μ.[32] Greater changes in charge carrier density up to 5×10^{13} $e^-\ cm^{-2}$ were observed when interfacing MoS_2 with a reduced form of benzyl viologen (BV) film, which was accompanied by a major increase in field-effect mobility. However, the BV doping of MoS_2 was accompanied by a semiconductor-to-semimetal phase transition, as evidenced by a loss in the field-effect modulation.[33] In our case, the vdWHs' FET devices could maintain a good I_{on}/I_{off} ratio, which increased from 9.9×10^5 to 2.8×10^6 with 2D-COF TAPB-PDA's dressing, and from 1.2×10^6 to 7.4×10^6 with 2D-COF TAPB-TFPB's interfacing. By and large, the mobility of our MoS_2 FET devices displayed a substantial increase upon interfacing with 2D-COF film, while a not enormous charge carrier density change of 10^{12} $e^-\ cm^{-2}$ enabled to retain MoS_2's semiconductor properties.

2.4. Monitoring the Optical Phonon Energy in vdWHs

High energy phonon ar known to scatter free carriers, thus affecting the carrier mobility of semiconductors.[34] Compared to the molecule assembly systems, the 2D-COFs have good robustness and stiffness, which can further improve MoS_2's charge carrier mobility by minimizing the coupling between phonons and electrons.

The optical phonon energies of MoS_2 and MoS_2/2D-COF heterostructures have been quantified by temperature-dependent PL spectra measured above 160 K.[35] **Figure 4**a showed that spectra of CVD MoS_2 monolayers transferred onto the Si/SiO_2 substrates at increasing temperature exhibit a blue shift of both A and B exciton peaks and decreased peak intensity. The A-exciton peaks could be extracted after the detailed Lorentzian

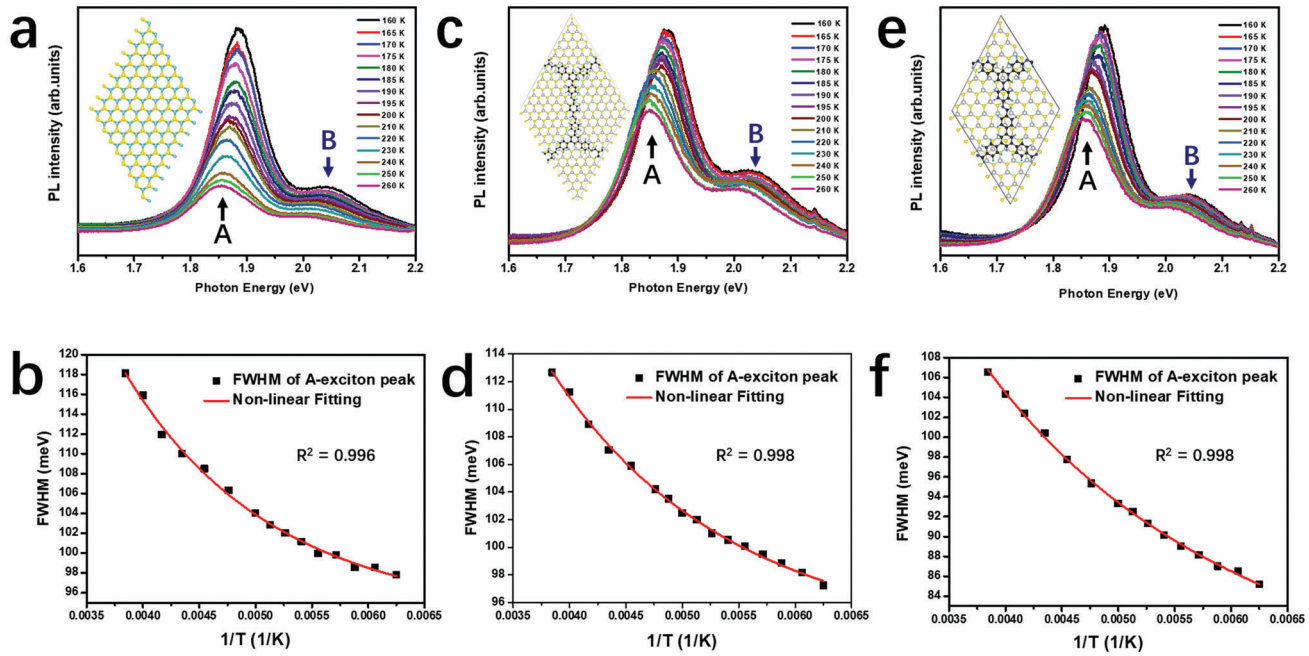

Figure 4. Temperature-dependent PL spectra and plotted FWHM: a,b) MoS_2, c,d) MoS_2/2D-COF TAPB-PDA heterostructure, and e,f) MoS_2/2D-COF TAPB-TFPB heterostructure.

fitting of PL spectra, e.g., the monolayer MoS_2 PL spectra at 160 K (Figure S25, Supporting Information). Meanwhile, the temperature-dependent peak-width broadening of A-exciton is plotted in Figure 4b and fitted using the independent Boson model.[36] The contribution of acoustic phonon could be neglected within the temperature range from 160 to 260 K, therefore the optical phonon dominates the line width broadening. Accordingly, the measured full-width at half-maxima (FWHM) data were fitted with the independent Boson model (Equation (3)), and the optical phonon energy was found as $\hbar\omega_{op} = 61.8 \pm 6.0$ meV. Our results were in excellent agreement with those obtained through theoretical calculation.[37] The temperature-dependent PL measurements were also carried out on the MoS_2/2D-COF vdWHs, as portrayed in Figure 4c,e. Compared to monolayer MoS_2, the heterostructure displayed a reduced decrease in the PL spectra intensity. More importantly, a significant reduction of $\hbar\omega_{op}$ was found after coated with 2D-COF film, as 48.2 ± 4.6 meV for MoS_2/2D-COF TAPB-PDA (Figure 4d) and 32.6 ± 7.1 meV for MoS_2/2D-COF TAPB-TFPB (Figure 4f). The decrease in the optical phonon energy represents a strong evidence for the suppression of the lattice vibration in MoS_2, which also indicates the suppression of phonon–electron interaction.[34b] In the vdWHs, the difference in 2D-COF structure yielded a different density of COFs' molecules on MoS_2. Notably, 2D-COF TAPB-TFPB film with a smaller porous size had a stronger suppression effect on MoS_2's lattice vibration, which could be related to a space confinement effect due to a large surface coverage.

The related activation energy of A-exciton (E_B) was obtained via Arrhenius equation, detailed in Figure S26 in the Supporting Information. A substantial drop of E_B after coating 2D-COF film could lead an increase in the free carrier population of MoS_2. As MoS_2/2D-COF heterostructures belonged to type II band alignment (Figure S13, Supporting Information), a depletion region of mobile charge carriers was formed at the interface, which caused dissociation in the electron and hole energy levels on both side of the junction, resulting in a reduced exciton energy state compared to pristine MoS_2 crystal.

2.5. Temperature-Dependent Carrier Transport in vdWHs FET

Carrier scattering, originated from deviations from ideal lattice periodicity, can act as a damping process for carrier motion: ionized impurity scattering in low-temperature range and lattice (phonon) scattering in high-temperature range are the two main phenomena.[38] To gain a deeper understanding on the scattering mechanism of electrons in our system, temperature-dependent mobility characteristics have been investigated.

Figure 5a displays the transfer characteristics of MoS_2 device measured from 10 to 300 K. The device transfer curves are expressed in terms of the channel conductivity ($\sigma = I_{DS} \times W/L$) to facilitate the comparison with the vdWH-FET devices. With the increasing temperature, the threshold voltage shifted toward negative values and the transfer current first increased then decreased.[39] The corresponding mobility (μ) as a function of temperature is plotted in Figure 5b: the mobility increased with the decreasing temperature in the temperature range from 300 to 100 K and almost saturated below 100 K, in agreement with previous studies.[34c,39c] The ionized impurity scattering in the pristine MoS_2 at temperatures below 200 K could be neglected. However, the mobility due to thermal lattice vibration scattering decreased with increasing tempera-

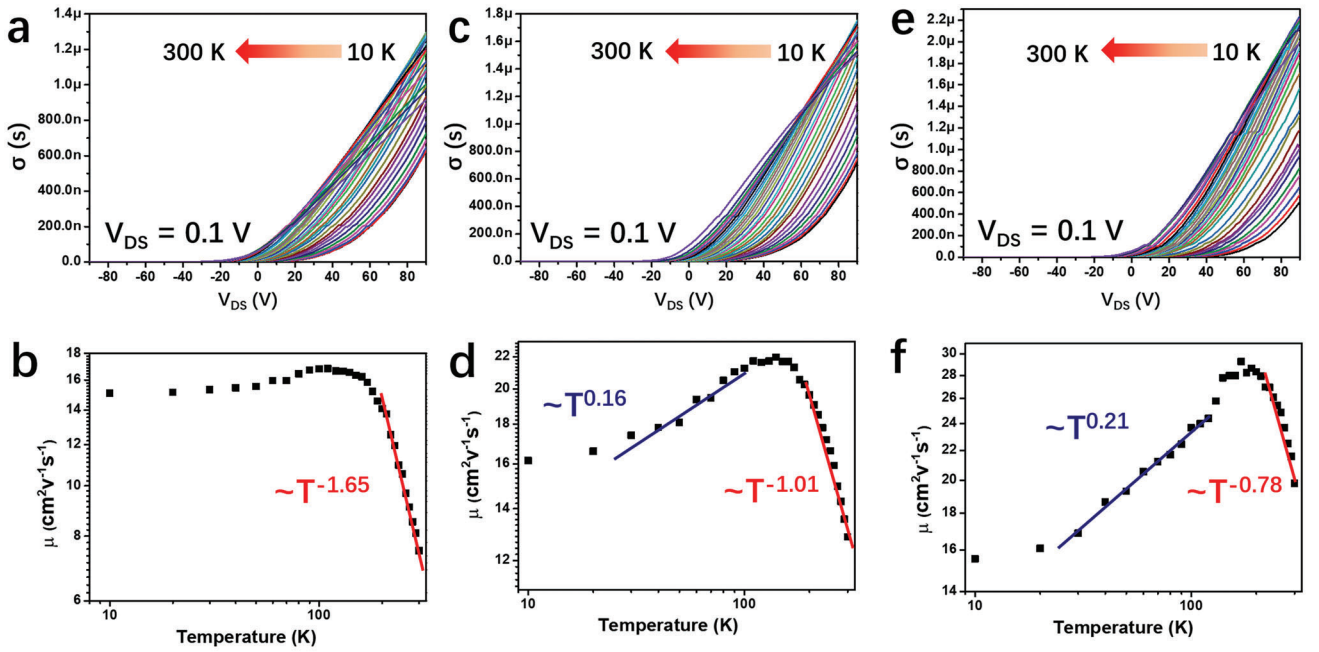

Figure 5. a) Temperature-dependent FET transfer curves of pristine monolayer MoS_2. b) The mobility related to a) as a function of temperature. c) Temperature-dependent FET transfer curves of MoS_2/2D-COF TAPB-PDA heterostructure. d) The mobility related to c) as a function of temperature. e) Temperature-dependent FET transfer curves of MoS_2/2D-COF TAPB-TFPB heterostructure. f) The mobility related to e) as a function of temperature.

ture, as the phonon population follows the Bose–Einstein distribution. Figure 5b revealed that mobility (μ) evolution in the temperature region from 200 to 300 K approximately folloeds the relation $\mu \propto T^{-\gamma}$, with $\gamma \sim 1.65$ being the phonon damping factor for pristine MoS_2 FET.[40]

The temperature-dependent transfer characteristics of MoS_2/2D-COF vdWHs were depicted in Figure 5c,e. Compared with the pristine MoS_2 device, the channel conductivity of the heterostructure displayed a significant improvement. Moreover, the mobilities of the heterostructure devices (Figure 5d,f) also increased with the decreasing temperature from 300 to 100 K. However, the increase in the device mobility for heterostructure was more reduced when compared to the pristine MoS_2 device, as confirmed by a smaller fitted γ (≈1.01 for MoS_2/2D-COF TAPB-PDA and ≈0.78 for MoS_2/2D-COF TAPB-TFPB). Since the carrier mobility was dominated by the intensity of lattice (phonon) scattering in high-temperature region, a small phonon damping factor (γ) could induce a high carrier mobility at room temperature.[39b] MoS_2/2D-COF TAPB-TFPB vdWH yielded a more efficient suppression on MoS_2's lattice vibration, in excellent agreement with the optical phonon energy results shown in Figure 4.

The doping of MoS_2 with organic molecules always generates charged dopants that hinder charge transport. The charged impurity scattering was observed in the MoS_2/2D-COF vdWHs devices.[41] Unlike the saturated case for pristine MoS_2, μ reached a maximum value at ≈150 K, and gradually slipped down at a temperature range below 100 K, in accordance with the power function ($\mu \propto T^{-\gamma}$) with a negative value of γ. More specifically, γ was fitted as ≈0.16 for MoS_2/2D-COF TAPB-PDA device (Figure 5d) and ≈0.21 for MoS_2/2D-COF TAPB-TFPB device (Figure 5f), coinciding quite well with the stronger electron doping effect in MoS_2/2D-COF TAPB-PDA device. All the mobility behaviors implied the suppression of lattice scattering in high-temperature range and the enhanced dopant-induced scattering in low-temperature range for the vdWH devices.[42]

3. Conclusion

In this work, we demonstrated the fabrication of hybrid MoS_2/2D-COF vdWHs by dressing monolayer CVD MoS_2 with 2D-COF films, by achieving a long-range order functionalization of MoS_2 with strong interlayer coupling effects, leading to significantly improved charge transport properties of MoS_2. Optical and electrical analyses corroborated with DFT calculations revealed that the 2D-COF induces a charge transfer process to MoS_2. Through the spatially long-range-ordered doping, the excess electrons transferred into the MoS_2 channel caused an enlargement in the free carriers' population by 10^{12} e^- cm^{-2}. Moreover, the 2D-COF film led confinement effect to reduce the lattice vibration of MoS_2, which were confirmed via temperature-dependent optical and electrical characterizations. The optical phonon energy of MoS_2 almost halved in the case of MoS_2/2D-COF TAPB-TFPB vdWH, while the device's mobility in room temperature increased by four times.

Using 2D-COF film to periodically dope TMDCs provided a novel approach to developing high-performance TMDC electronics. Based on the large library of organic functional molecules, the 2D-COF structure could be ad hoc designed, e.g., with 2D-COF structures incorporating n-doped monomers to further boost the n-doping effect for high-performance (opto)electronics or responsive building blocks to impart responsiveness to multiple external stimuli, for application in light-sensing and photodetection. Moreover, the mechanical stiffness and thermal dy-

namic stability of the 2D-COF opens perspectives toward the use of the novel vdWH in artificial e-skins and ultraflexible devices for health monitoring and related smart technologies.

4. Experimental Section

STM and AFM: STM measurements were performed by a Veeco scanning tunneling microscope (multimode Nanoscope III, Veeco). 200 nm thick Au (111) on mica was used as substrate for 2D-COF film coating. The employed STM tips were mechanically cut from a Pt/Ir wire (80/10, diameter 0.25 mm). The images were captured under ambient conditions. AFM images were obtained using a Bruker Dimension Icon set-up operating in air, in tapping mode, by using tip model TESPA-V2, tip stiffness K is 42 N m^{-1}.

XPS: XPS analyses were carried out with a Thermo Scientific K-Alpha X-ray photoelectron spectrometer. A basic chamber pressure was about 10^{-9} mbar. Aluminum anode was employed as the X-ray source (X-ray radiation of 1486 eV). All XPS spectra were calibrated using the C 1s peak at 284.8 eV as a reference. Peak-fitting and chemical qualification were performed using the Avantage software.

FET Fabrication and Characterization: CVD MoS_2 flakes (Six Carbon Technology) were transferred onto SiO_2 substrates (270 nm SiO_2 thickness onto n-doped Si from Fraunhofer IPMS, Germany). Back-gated FET devices were fabricated by laser writer lithography, with Au source and drain electrodes thermally evaporated onto the patterned substrate. Warm acetone was used for the lift-off process, and the as-fabricated devices were annealed at 390 K in vacuum to remove atmospheric adsorbates. The fabricated FET devices were measured in an N_2-filled glovebox with a probe station connected to a Keithley 2636A source-meter unit.

Temperature-dependent measurements were carried out in a cryogenic probe station (Janis-CCR5-2) using a semiconductor parameter analyzer (Keithley 4200) with a vacuum degree of about 5×10^{-5} mbar.

The carrier mobility μ was determined from the following equation:

$$\mu = \frac{dI_{DS}}{dV_{DS}} \times \frac{L}{WC_i V_{DS}} \tag{1}$$

where L and W are the channel length and width, and C_i is the insulator capacitance per unit of area.

The dopant-induced charge carrier density increase (Δn) was calculated from Equation (2):

$$\Delta n = C_i \frac{\Delta V_{th}}{e} \tag{2}$$

where ΔV_{th} is the difference in threshold voltage (V_{th}) before and after doping effect and e is the elementary charge (1.6×10^{-19} C).

Raman and PL Spectra: Raman and PL spectra were carried out in air by Renishaw inVia spectrometer equipped with 532 nm laser, and the wavenumber resolution was 1 cm^{-1}. The excitation power was kept below 1 mW to avoid the local heating damaged effects. Temperature-dependent experiments were recorded with the samples protected under inert nitrogen atmosphere, and low temperatures were applied with a Linkam TP95 temperature controller.

The independent Boson model equation was as follows:

$$\Gamma\ (T) = \Gamma_0\ + \sigma T + \frac{\Gamma_o p}{e^{\hbar\omega_o p/k_B T} - 1} \tag{3}$$

in which Γ_0 is the inhomogenous broadening contribution, σ is the exciton-acoustic phononinteraction ($T > 0$, neglected), $\Gamma_o p$ is the exciton-optical phonon contribution, K_B is the Boltzmann constant (8.617×10^{-5} eV K^{-1}), and $\hbar\omega_0 p$ is the optical phonon energy.

DFT Calculations: Charge density calculations were performed by using the Vienna ab-initio Simulation Package (VASP).[43] The Perdew–Burke–Ernzerhof[44] functional was used to describe electron exchange and correlation. DFT-D2 method of Grimme[45] was used in order to describe van der Waals forces. The Bader technique[46] was adopted in order to determine the charge transfer in the structure. The kinetic energy cut-off for plane-wave expansion was set to 400 eV and the energy was minimized until its variation in the following steps became 10^{-4} eV. The Gaussian smearing method was employed for the total energy calculations and the width of the smearing was chosen as 0.05 eV. Total Hellmann–Feynman forces in the unit were reduced to 10^{-3} eV $Å^{-1}$. (1,1,1) Γ-centered k-point samplings were used for the unit cells. 3000 grid points were used for electronic density of states calculations.

Supporting Information

Supporting Information is available from the Wiley Online Library or from the author.

Acknowledgements

The authors acknowledge funding from the European Commission through the ERC project SUPRA2DMAT (GA-833707), the Graphene Flagship Core 3 project (GA-881603), and the Marie Sklodowska-Curie project ULTIMATE (GA-813036) as well as the Agence Nationale de la Recherche through the Interdisciplinary Thematic Institute SysChem via the IdEx Unistra (ANR-10-IDEX-0002) within the program Investissement d'Avenir, the International Center for Frontier Research in Chemistry (icFRC), and the Institut Universitaire de France (IUF). The authors are greatful to the support from Center for Information Services and High Performance Computing (ZIH), TU Dresden, Dresden, Germany. The authors also acknowledge the funding from Department of Science and Technology of Jilin Province (20230508176RC), and the support from Dingxin Scholar program, Jilin University, China.

Conflict of Interest

The authors declare no conflict of interest.

Data Availability Statement

The data that support the findings of this study are available from the corresponding author upon reasonable request.

Keywords

2D covalent organic frameworks, charge transport, interface engineering, transition metal dichalcogenides, van der Waals heterostructures

Received: June 18, 2023
Revised: August 23, 2023
Published online: November 23, 2023

[1] a) M. Chhowalla, H. S. Shin, G. Eda, L.-J. Li, K. P. Loh, H. Zhang, *Nat. Chem.* **2013**, *5*, 263; b) Q. H. Wang, K. Kalantar-Zadeh, A. Kis, J. N. Coleman, M. S. Strano, *Nat. Nanotechnol.* **2012**, *7*, 699.
[2] Y. Zhao, M. Gobbi, L. E. Hueso, P. Samorì, *Chem. Rev.* **2022**, *122*, 50.
[3] L. Cheng, Y. Liu, *J. Am. Chem. Soc.* **2018**, *140*, 17895.
[4] a) Z. Yu, Z.-Y. Ong, S. Li, J.-B. Xu, G. Zhang, Y.-W. Zhang, Y. Shi, X. Wang, *Adv. Funct. Mater.* **2017**, *27*, 1604093; b) S. Das, A. Sebastian, E. Pop, C. J. Mcclellan, A. D. Franklin, T. Grasser, T. Knobloch, Y. Illarionov, A. V. Penumatcha, J. Appenzeller, Z. Chen, W. Zhu, I. Asselberghs, L.-J. Li, U. E. Avci, N. Bhat, T. D. Anthopoulos, R. Singh, *Nat. Electron.* **2021**, *4*, 786.

[5] a) L. Banszerus, M. Schmitz, S. Engels, J. Dauber, M. Oellers, F. Haupt, K. Watanabe, T. Taniguchi, B. Beschoten, C. Stampfer, *Sci. Adv.* **2015**, *1*, e1500222; b) J. Tang, Q. Wang, Z. Wei, C. Shen, X. Lu, S. Wang, Y. Zhao, J. Liu, N. Li, Y. Chu, J. Tian, F. Wu, W. Yang, C. He, R. Yang, D. Shi, K. Watanabe, T. Taniguchi, G. Zhang, *Adv. Electron. Mater.* **2020**, *6*, 2000550.

[6] B. Radisavljevic, A. Radenovic, J. Brivio, V. Giacometti, A. Kis, *Nat. Nanotechnol.* **2011**, *6*, 147.

[7] D. Li, R. Cheng, H. Zhou, C. Wang, A. Yin, Y. Chen, N. O. Weiss, Y. Huang, X. Duan, *Nat Commun* **2015**, *6*, 7509.

[8] Y. Y. Illarionov, A. G. Banshchikov, D. K. Polyushkin, S. Wachter, T. Knobloch, M. Thesberg, L. Mennel, M. Paur, M. Stöger-Pollach, A. Steiger-Thirsfeld, M. I. Vexler, M. Waltl, N. S. Sokolov, T. Mueller, T. Grasser, *Nat. Electron.* **2019**, *2*, 230.

[9] a) Y. Li Huang, Y. J. Zheng, Z. Song, D. Chi, A. T. S. Wee, S. Y. Quek, *Chem. Soc. Rev.* **2018**, *47*, 3241; b) K. Pei, T. Zhai, *Cell Rep. Phys. Sci.* **2020**, *1*, 100166.

[10] C. Wang, R. Furlan De Oliveira, K. Jiang, Y. Zhao, N. Turetta, C. Ma, B. Han, H. Zhang, D. Tranca, X. Zhuang, L. Chi, A. Ciesielski, P. Samorì, *Nat. Commun.* **2022**, *13*, 510.

[11] a) T. Kudernac, S. Lei, J. A. A. W. Elemans, S. De Feyter, *Chem. Soc. Rev.* **2009**, *38*, 402; b) R. Gutzler, T. Sirtl, J. F. Dienstmaier, K. Mahata, W. M. Heckl, M. Schmittel, M. Lackinger, *J. Am. Chem. Soc.* **2010**, *132*, 5084.

[12] a) F. Haase, B. V. Lotsch, *Chem. Soc. Rev.* **2020**, *49*, 8469; b) A. M. Evans, M. J. Strauss, A. R. Corcos, Z. Hirani, W. Ji, L. S. Hamachi, X. Aguilar-Enriquez, A. D. Chavez, B. J. Smith, W. R. Dichtel, *Chem. Rev.* **2022**, *122*, 442.

[13] Y. Jin, Y. Hu, M. Ortiz, S. Huang, Y. Ge, W. Zhang, *Chem. Soc. Rev.* **2020**, *49*, 4637.

[14] a) Y. Wu, H. Xu, X. Chen, J. Gao, D. Jiang, *Chem. Commun.* **2015**, *51*, 10096; b) X. Ding, X. Feng, A. Saeki, S. Seki, A. Nagai, D. Jiang, *Chem. Commun.* **2012**, *48*, 8952.

[15] S. Wan, F. Gándara, A. Asano, H. Furukawa, A. Saeki, S. K. Dey, L. Liao, M. W. Ambrogio, Y. Y. Botros, X. Duan, S. Seki, J. F Stoddart, O. M. Yaghi, *Chem. Mater.* **2011**, *23*, 4094.

[16] a) X. Li, P. Yadav, K. P. Loh, *Chem. Soc. Rev.* **2020**, *49*, 4835; b) H. Sahabudeen, H. Qi, B. A. Glatz, D. Tranca, R. Dong, Y. Hou, T. Zhang, C. Kuttner, T. Lehnert, G. Seifert, U. Kaiser, A. Fery, Z. Zheng, X. Feng, *Nat. Commun.* **2016**, *7*, 13461.

[17] a) H. B. Balch, A. M. Evans, R. R. Dasari, H. Li, R. Li, S. Thomas, D. Wang, R. P. Bisbey, K. Slicker, I. Castano, S. Xun, L. Jiang, C. Zhu, N. Gianneschi, D. C. Ralph, J.-L. Brédas, S. R. Marder, W. R. Dichtel, F. Wang, *J. Am. Chem. Soc.* **2020**, *142*, 21131; b) A. M. Evans, A. Giri, V. K. Sangwan, S. Xun, M. Bartnof, C. G. Torres-Castanedo, H. B. Balch, M. S. Rahn, N. P. Bradshaw, E. Vitaku, D. W. Burke, H. Li, M. J. Bedzyk, F. Wang, J.-L. Brédas, J. A. Malen, A. J. H. Mcgaughey, M. C. Hersam, W. R. Dichtel, P. E. Hopkins, *Nat. Mater.* **2021**, *20*, 1142.

[18] a) L. Wang, H. Sahabudeen, T. Zhang, R. Dong, *npj 2D Mater. Appl.* **2018**, *2*, 26; b) D. B. Shinde, G. Sheng, X. Li, M. Ostwal, A.-H. Emwas, K.-W. Huang, Z. Lai, *J. Am. Chem. Soc.* **2018**, *140*, 14342.

[19] T. Gunst, T. Markussen, K. Stokbro, M. Brandbyge, *Phys. Rev. B* **2016**, *93*, 035414.

[20] a) L. Zhai, N. Huang, H. Xu, Q. Chen, D. Jiang, *Chem. Commun.* **2017**, *53*, 4242; b) D. Kaleeswaran, P. Vishnoi, R. Murugavel, *J. Mater. Chem.* **2015**, *3*, 7159.

[21] S. Kim, H. Lim, J. Lee, H. C. Choi, *Langmuir* **2018**, *34*, 8731.

[22] K. Liu, J. Li, H. Qi, M. Hambsch, J. Rawle, A. R. Vázquez, A. S. Nia, A. Pashkin, H. Schneider, M. Polozij, T. Heine, M. Helm, S. C. B. Mannsfeld, U. Kaiser, R. Dong, X. Feng, *Angew. Chem., Int. Ed.* **2021**, *60*, 13859.

[23] S. Kim, H. C. Choi, *Commun. Chem.* **2019**, *2*, 60.

[24] L. Chen, X. Gu, M. J. Fasolka, J. W. Martin, T. Nguyen, *Langmuir* **2009**, *25*, 3494.

[25] a) C. Fan, H. Wu, J. Guan, X. You, C. Yang, X. Wang, L. Cao, B. Shi, Q. Peng, Y. Kong, Y. Wu, N. A. Khan, Z. Jiang, *Angew. Chem., Int. Ed.* **2021**, *60*, 18051; b) C. Yuan, X. Wu, R. Gao, X. Han, Y. Liu, Y. Long, Y. Cui, *J. Am. Chem. Soc.* **2019**, *141*, 20187.

[26] Y. Hu, N. Goodeal, Y. Chen, A. M. Ganose, R. G. Palgrave, H. Bronstein, M. O. Blunt, *Chem. Commun.* **2016**, *52*, 9941.

[27] a) W. Dai, F. Shao, J. Szczerbinski, R. Mccaffrey, R. Zenobi, Y. Jin, A. D Schlüter, W. Zhang, *Angew. Chem., Int. Ed.* **2016**, *55*, 213; b) F. Shao, W. Dai, Y. Zhang, W. Zhang, A. D. Schlüter, R. Zenobi, *ACS Nano* **2018**, *12*, 5021.

[28] A. Gurarslan, Y. Yu, L. Su, Y. Yu, F. Suarez, S. Yao, Y. Zhu, M. Ozturk, Y. Zhang, L. Cao, *ACS Nano* **2014**, *8*, 11522.

[29] a) S. Zhang, H. M. Hill, K. Moudgil, C. A. Richter, A. R. Hight Walker, S. Barlow, S. R. Marder, C. A. Hacker, S. J. Pookpanratana, *Adv. Mater.* **2018**, *30*, 1802991; b) A. Splendiani, L. Sun, Y. Zhang, T. Li, J. Kim, C.-Y. Chim, G. Galli, F. Wang, *Nano Lett.* **2010**, *10*, 1271; c) H. Li, Q. Zhang, C. C. R. Yap, B. K. Tay, T. H. T. Edwin, A. Olivier, D. Baillargeat, *Adv. Funct. Mater.* **2012**, *22*, 1385.

[30] a) K. F. Mak, K. He, C. Lee, G. H. Lee, J. Hone, T. F. Heinz, J. Shan, *Nat. Mater.* **2013**, *12*, 207; b) H.-V. Han, A.-Yu Lu, L.-S. Lu, J.-K. Huang, H. Li, C.-L. Hsu, Y.-C. Lin, M.-H. Chiu, K. Suenaga, C.-W. Chu, H.-C. Kuo, W.-H. Chang, L.-J. Li, Y. Shi, *ACS Nano* **2016**, *10*, 1454; c) J. S. Ross, S. Wu, H. Yu, N. J. Ghimire, A. M. Jones, G. Aivazian, J. Yan, D. G. Mandrus, D. Xiao, W. Yao, X. Xu, *Nat. Commun.* **2013**, *4*, 1474.

[31] a) B. Lei, Y. Pan, Z. Hu, J. Zhang, D. Xiang, Y. Zheng, R. Guo, C. Han, L. Wang, J. Lu, L. Yang, W. Chen, *ACS Nano* **2018**, *12*, 2070; b) B. Chamlagain, S. S. Withanage, A. C. Johnston, S. I. Khondaker, *Sci. Rep.* **2020**, *10*, 12970.

[32] a) M. Gobbi, S. Bonacchi, J. X. Lian, A. Vercouter, S. Bertolazzi, B. Zyska, M. Timpel, R. Tatti, Y. Olivier, S. Hecht, M. V. Nardi, D. Beljonne, E. Orgiu, P. Samorì, *Nat. Commun.* **2018**, *9*, 3689; b) Y. Zhao, S. Bertolazzi, P. Samorì, *ACS Nano* **2019**, *13*, 4814.

[33] M. Yarali, Y. Zhong, S. N. Reed, J. Wang, K. A. Ulman, D. J. Charboneau, J. B. Curley, D. J. Hynek, J. V. Pondick, S. Yazdani, N. Hazari, S. Y. Quek, H. Wang, J. J. Cha, *Adv. Electron. Mater.* **2021**, *7*, 2000873.

[34] a) D. K. Efetov, P. Kim, *Phys. Rev. Lett.* **2010**, *105*, 256805; b) Y. Nakamura, T. Zhao, J. Xi, W. Shi, D. Wang, Z. Shuai, *Adv. Electron. Mater.* **2017**, *3*, 1700143; c) D. Lee, J. J. Lee, Y. S. Kim, Y. H. Kim, J. C. Kim, W. Huh, J. Lee, S. Park, H. Y Jeong, Y. D. Kim, C.-H. Lee, *Nat. Electron.* **2021**, *4*, 664.

[35] a) H. Li, X. H. Zhang, *Opt. Mater.* **2020**, *107*, 110150; b) K. Wu, A. Bera, C. Ma, Y. Du, Y. Yang, L. Li, T. Wu, *Phys. Chem. Chem. Phys.* **2014**, *16*, 22476.

[36] S. Rudin, T. L. Reinecke, B. Segall, *Phys. Rev. B* **1990**, *42*, 11218.

[37] a) F. Caruso, P. Amsalem, J. Ma, A. Aljarb, T. Schultz, M. Zacharias, V. Tung, N. Koch, C. Draxl, *Phys. Rev. B* **2021**, *103*, 205152; b) A. Molina-Sánchez, L. Wirtz, *Phys. Rev. B* **2011**, *84*, 155413.

[38] a) S.-J. Lee, Z. Lin, X. Duan, Y. Huang, *Nat. Electron.* **2020**, *3*, 77; b) W. Shi, S. Kahn, L. Jiang, S.-Y. Wang, H.-Z. Tsai, D. Wong, T. Taniguchi, K. Watanabe, F. Wang, M. F. Crommie, A. Zettl, *Nat. Electron.* **2020**, *3*, 99.

[39] a) X. Liu, J. He, Q. Liu, D. Tang, J. Wen, W. Liu, W. Yu, J. Wu, Z. He, Y. Lu, D. Zhu, W. Liu, P. Cao, S. Han, K.-W. Ang, *J. Appl. Phys.* **2015**, *118*, 124506; b) B. Radisavljevic, A. Kis, *Nat. Mater.* **2013**, *12*, 815; c) D. Jariwala, V. K. Sangwan, D. J. Late, J. E. Johns, V. P. Dravid, T. J. Marks, L. J. Lauhon, M. C. Hersam, *Appl. Phys. Lett.* **2013**, *102*, 173107.

[40] K. Kaasbjerg, K. S. Thygesen, K. W. Jacobsen, *Phys. Rev. B* **2012**, *85*, 115317.

[41] D. Long, J. Myers, *Phys. Rev.* **1959**, *115*, 1107.
[42] a) S. Kim, A. Konar, W.-S. Hwang, J. H. Lee, J. Lee, J. Yang, C. Jung, H. Kim, J.-B. Yoo, J.-Y. Choi, Y. W. Jin, S. Y. Lee, D. Jena, W. Choi, K. Kim, *Nat. Commun.* **2012**, *3*, 1011; b) J. Jang, J.-K. Kim, J. Shin, J. Kim, K.-Y. Baek, J. Park, S. Park, Y. D. Kim, S S. P. Parkin, K. Kang, K. Cho, T. Lee, *Sci. Adv.* **2022**, *8*, eabn3181.
[43] a) G. Kresse, J. Hafner, *Phys. Rev. B* **1993**, *47*, 558; b) G. Kresse, J. Furthmüller, *Phys. Rev. B* **1996**, *54*, 11169.
[44] J. P. Perdew, K. Burke, M. Ernzerhof, *Phys. Rev. Lett.* **1996**, *77*, 3865.
[45] S. Grimme, *J. Comput. Chem.* **2006**, *27*, 1787.
[46] G. Henkelman, A. Arnaldsson, H. Jónsson, *Comput. Mater. Sci.* **2006**, *36*, 354.